



Cite this: *EES Catal.*, 2024, 2, 1092

Received 15th May 2024,
Accepted 10th June 2024

DOI: 10.1039/d4ey00106k

rsc.li/eescatalysis

Surface amorphization and functionalization of a NiFeOOH electrocatalyst for a robust seawater electrolyzer†

Hao Wang,^{a,c} Nannan Jiang,^a Bing Huang,^a Qiangmin Yu^{*b} and Lunhui Guan^{ID, *a}

Hydrogen production of seawater electrolysis has attracted considerable interest due to the abundant seawater resources. However, the chloride ions (Cl^-) in seawater not only corrode the electrodes but also cause side reactions, severely impacting the electrode efficiency and stability of the oxygen evolution reaction (OER) in seawater electrolysis. These challenges are the key factors limiting the development of seawater electrolysis technology. Here, we developed a surface-functionalized high-performance catalyst, which not only resists Cl^- corrosion using surface-functionalized ions, but also improves the OER activity by surface amorphization. The designed catalyst ($\text{Ru}_{0.1}\text{-NiFeOOH}/\text{PO}_4^{3-}$) is composed of $\text{Ru}_{0.1}\text{-NiFeOOH}$ and surface phosphate. On the one hand, a small amount of Ru doping can increase the surface amorphization of

NiFeOOH and thus improve the catalytic activity. On the other hand, the phosphates on $\text{Ru}_{0.1}\text{-NiFeOOH}$ are resistant to Cl^- corrosion, which in turn improves the electrode stability. This catalyst demonstrates robust performance operation over 1000 h in alkaline seawater solutions at an industrial current density of 0.5 A cm^{-2} . The anion exchange membrane seawater electrolyzer assembled with $\text{Ru}_{0.1}\text{-NiFeOOH}/\text{PO}_4^{3-}$ only needs 1.6 V to achieve 0.5 A cm^{-2} when powered by sustainable solar energy. The electrolyzer efficiency is 75.1% at 0.5 A cm^{-2} , which is superior to the 2030 technical target of 65% set by the U.S. DOE and most reported work. This work offers a new perspective for designing efficient and stable catalysts and is of great significance for advancing seawater electrolysis technology.

Broader context

Hydrogen production by seawater electrolysis has gradually attracted considerable interest due to freshwater scarcity. However, the chloride ions (Cl^-) in seawater seriously affect the selectivity of the anode catalyst for the oxygen evolution reaction (OER) and the electrode lifetime. Transition metal hydroxyl oxides (M-OOH) are regarded as the active phase of the OER, which suffers from the problems of difficult exposure of internal active sites and poor resistance to Cl^- corrosion. Herein, we report the optimization of the active site structure through heteroatom doping to promote M-OOH surface amorphization coupled with surface functionalization to enhance the catalytic activity and Cl^- corrosion resistance of the catalyst. Meanwhile, experimental characterization combined with theoretical calculations demonstrated the effectiveness of the above strategies. This work provides a good reference for the rational design of effective and stable catalysts for seawater electrolysis.

Introduction

The overuse of fossil energy is causing an unprecedented energy and environmental crisis.¹ In response to this crisis, the scientific research and industrial sectors are accelerating

their search for sustainable, environmentally friendly, and low-carbon energy alternatives.² Among many candidates, hydrogen (H_2) energy, with pollution-free and high-efficiency properties, is the well-known ideal energy.^{3,4} H_2 produced by water electrolysis using renewable energy is a promising technology, which

^a State Key Laboratory of Structural Chemistry, Fujian Key Laboratory of Nanomaterials, and CAS Key Laboratory of Design and Assembly of Functional Nanostructures, Fujian Institute of Research on the Structure of Matter, Chinese Academy of Sciences, Fuzhou, Fujian 350002, China. E-mail: guanh@fjirsm.ac.cn

^b Shenzhen Geim Graphene Center, Tsinghua-Berkeley Shenzhen Institute & Institute of Materials Research, Tsinghua Shenzhen International Graduate School, Tsinghua University, Shenzhen 518055, P. R. China. E-mail: yu.qiangmin@sz.tsinghua.edu.cn

^c College of Chemistry, Fuzhou University, Fuzhou 350108, China

† Electronic supplementary information (ESI) available. See DOI: <https://doi.org/10.1039/d4ey00106k>



is favorable to energy and environmental sustainability.^{5,6} In the backdrop of increasing global freshwater scarcity, the exploitation of seawater, which constitutes 96.5% of the water resources, emerges as a potential hydrogen-containing resource.⁷ Meanwhile, combining seawater electrolysis with solar energy is a more promising technology for green H₂ production.⁸ However, the inorganic salt, especially chloride ions in seawater, will corrode the electrode substrate and active sites of the catalysts.⁹ Currently, seawater electrolysis is divided into desalination followed by electrolysis and direct electrolysis.^{10,11} Xie *et al.* used a waterproof breathable membrane to achieve the separation of water and ions, while it shows poor performance at high current densities due to the insufficient supply of water to the system.¹² Direct seawater electrolysis will allow chloride ions (Cl⁻) to be adsorbed on the electrode surface, resulting in the electrode being corroded. In addition, the chlorine evolution reaction will be triggered under high applied potentials. Therefore, it is urgent to develop

corrosion-resistant and high-performance catalysts to reduce the electrode degradation and improve the oxygen evolution reaction (OER) selectivity, while such catalysts have not yet been developed.¹³

Recently, transition metal-based catalysts especially layered double hydroxides (LDHs), are increasingly valued for their low cost, high efficiency and environmental benefits.¹⁴⁻¹⁷ However, Cl⁻ may promote the corrosion of metal ions on the surface of LDHs, leading to active site destruction. Yu *et al.* used CoCu LDH doped with heteroatoms (Ni, Fe) to split seawater. The heteroatom doped CoCu LDH shows a low overpotential of 315 mV at 100 mA cm⁻², but the stability was limited to 50 h due to the Cl⁻ corroding the electrodes.¹⁸ Consequently, the LDHs need to be modified to improve their corrosion-resistance. Shao *et al.* modified NiFe LDH with molybdate (MoO₄²⁻). The modified NiFe LDH showed excellent stability of 550 h but a large overpotential of 332 mV at 100 mA cm⁻².¹⁹

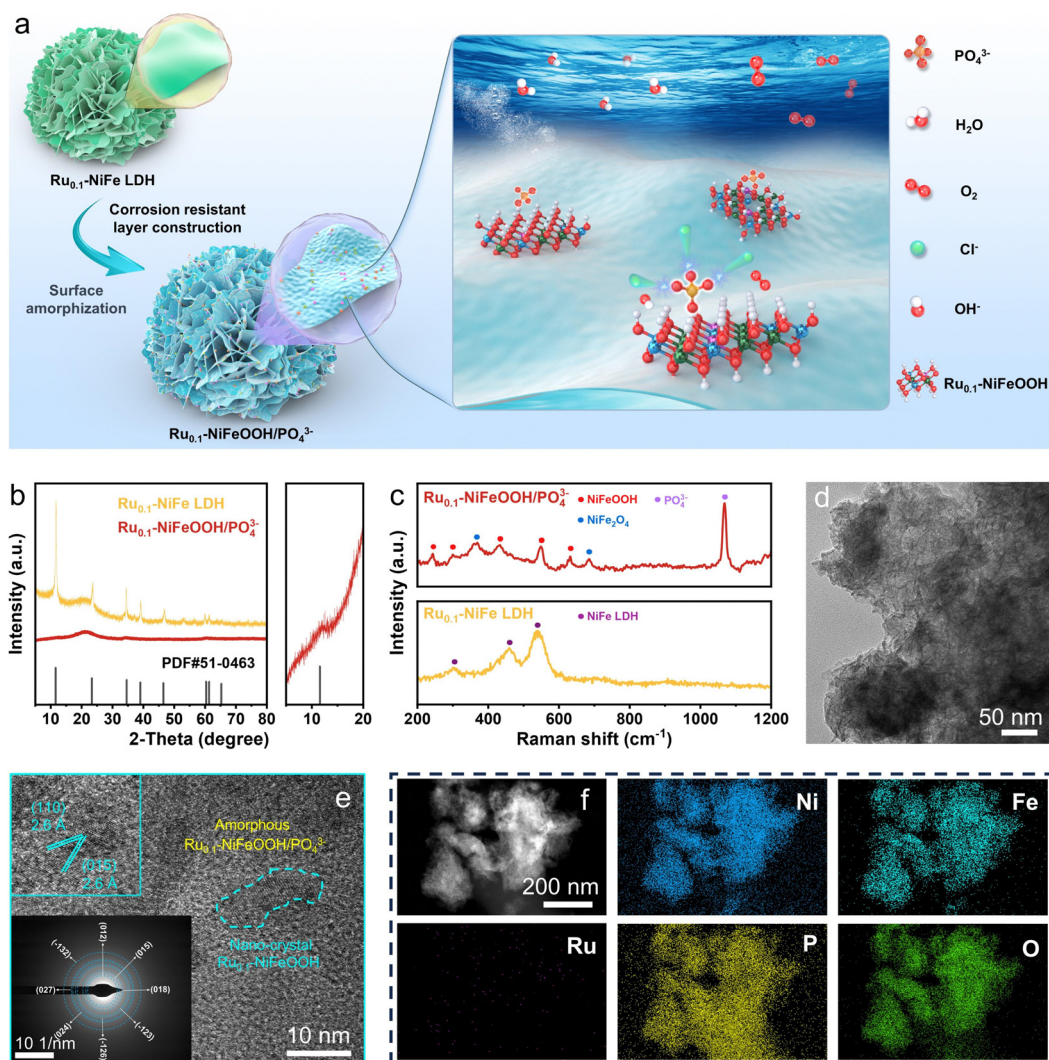


Fig. 1 (a) Schematic of the surface amorphization and functionalization process. (b) XRD patterns and (c) Raman spectra of Ru_{0.1}-NiFeOOH/PO₄³⁻ and Ru_{0.1}-NiFe LDH, respectively. (d) TEM image, (e) HR-TEM image with the selected area electron diffraction inset and (f) high-angle annular dark-field scanning transmission electron microscopy (HAADF-STEM) image with the corresponding elemental mappings of Ru_{0.1}-NiFeOOH/PO₄³⁻.



These results show that the introduction of heteroatoms and anions can improve the activity and stability of the catalysts, respectively. Nevertheless, it is challenging to introduce high active sites in the electrode structure while guaranteeing its corrosion resistance of Cl^- .

Here, we designed a $\text{Ru}_{0.1}\text{-NiFeOOH/PO}_4^{3-}$ catalyst from the perspectives of surface amorphization and functionalization. Among them, Ru doping accelerated the amorphization process of the catalyst, thus enhancing the catalytic activity of the electrode. Meanwhile, the *in situ* generated PO_4^{3-} exhibits electrostatic repulsion against Cl^- in seawater, improving the corrosion-resistance ability of the electrode. The results demonstrate that this strategy enables $\text{Ru}_{0.1}\text{-NiFeOOH/PO}_4^{3-}$ to exhibit a low overpotential of 255 mV under 10 mA cm^{-2} in seawater electrolyte. Moreover, the catalyst operates stably at 0.5 A cm^{-2} in seawater electrolytes over 1000 h. Notably, we assembled the $\text{Ru}_{0.1}\text{-NiFeOOH/PO}_4^{3-}$ catalyst in an anion exchange membrane (AEM) electrolyzer and powered it by solar energy. This electrolyzer requires only 1.6 V to achieve 0.5 A cm^{-2} . These results indicate that the strategy of surface amorphization paired with functionalization enables the catalyst to exhibit excellent catalytic activity and stability. This work not only addresses the technical challenges in seawater electrolysis, but also provides an economical and feasible solution for H_2 production with rich seawater and renewable energy.

Results and discussion

The $\text{Ru}_{0.1}\text{-NiFeOOH/PO}_4^{3-}$ catalyst was synthesized by an electrochemical activation strategy, while the compositional information of the pre-catalyst $\text{Ru}_{0.1}\text{-NiFeP}$ is shown in Fig. S1–S4 (ESI†). As illustrated in Fig. 1a, *in situ* generated PO_4^{3-} adsorbed on the surface of $\text{Ru}_{0.1}\text{-NiFeOOH}$, which can electrostatically repel Cl^- from seawater and avoid the active sites being corroded. Fig. 1b and Fig. S5 (ESI†) exhibit a phase transition from crystallization to amorphization between $\text{Ru}_{0.1}\text{-NiFe LDH}$ and $\text{Ru}_{0.1}\text{-NiFeOOH/PO}_4^{3-}$. Although the characteristic peak of NiFeOOH near 12° can still be observed, its crystallinity is quite low. Fig. S6 (ESI†) shows no peaks for Ni_2P and FeP , which confirms the absence of residual NiFeP . These findings show that the electrochemical activation strategy significantly destroys the NiFeOOH lattice, resulting in a high degree amorphization of the catalyst surface. In the Raman spectrum (Fig. 1c), the $\text{Ru}_{0.1}\text{-NiFeOOH/PO}_4^{3-}$ exhibits two characteristic peaks located at 248 and 306 cm^{-1} , corresponding to the Ni-O/Fe-O vibration modes in the NiFeOOH . The characteristic peaks at 430 , 554 , and 625 cm^{-1} are attributed to lattice vibrations of the NiFeOOH . Additionally, the characteristic peak at 1068 cm^{-1} corresponds to the PO_4^{3-} .²⁰ The literature indicates that the characteristic peaks at 365 and 699 cm^{-1} can be attributed to the NiFe_2O_4 spinel structure, which involves the evolution cycle of $\text{Ni}^{2+}/3+$ and $\text{Fe}^{2+}/3+$ active sites.²¹ These results reveal that the PO_4^{3-} functionalized $\text{Ru}_{0.1}\text{-NiFeOOH}$ electrode was prepared well. The transmission electron microscopy (TEM) image (Fig. 1d) shows that an

amorphous layer formed on $\text{Ru}_{0.1}\text{-NiFeOOH/PO}_4^{3-}$, further confirming its larger specific surface area compared to pre-activation. In contrast to the high crystallinity of $\text{Ru}_{0.1}\text{-NiFe LDH}$ (Fig. S7, ESI†), the high-resolution transmission electron microscopy (HR-TEM) image (Fig. 1e) shows the amorphization of $\text{Ru}_{0.1}\text{-NiFeOOH/PO}_4^{3-}$, with a few remaining NiFeOOH nanocrystals. The illustration in Fig. 1e shows the SAED pattern of $\text{Ru}_{0.1}\text{-NiFeOOH/PO}_4^{3-}$, displaying no diffraction spots. This indicates the absence of Ru metal particles or nanoclusters and suggests that Ru is incorporated as a dopant in the NiFeOOH structure. Energy dispersive spectroscopy (EDS) analysis indicates that Ni, Fe and Ru elements are homogeneously distributed over $\text{Ru}_{0.1}\text{-NiFeOOH/PO}_4^{3-}$ (Fig. 1f and Table S1, ESI†).

X-ray photoelectron spectroscopy (XPS) survey results indicate that the $\text{Ru}_{0.1}\text{-NiFeOOH/PO}_4^{3-}$ contains Ni, Fe, P and O, as well as trace Ru elements (Fig. S8, ESI†). High resolution XPS spectra of Ni 2p and Fe 2p (Fig. 2a and b) indicate that the characteristic peaks of Ni-P and Fe-P disappeared, and the peak of phosphates was observed after electrochemical activation (Fig. 2c and Fig. S9, ESI†).²² This result indicates that the $\text{Ru}_{0.1}\text{-NiFeOOH}$ catalyst is functionalized by the phosphates. For $\text{Ru}_{0.1}\text{-NiFeP}$, the peak at 129.5 eV is attributed to P-Ni/Fe, while the peak at 133.6 eV is attributed to the oxidized phosphate species.²³ In Fig. 2d, a shift of the Ru 3d_{5/2} peak from 361.3 eV to 362.2 eV is observed, demonstrating the generation of high-valence Ru. This leads to a decrease of Ru-O bond length, which promotes lattice distortion and accelerates the amorphization of the NiFeOOH surface.²⁴ Meanwhile, the content of oxygen vacancies on the $\text{Ru}_{0.1}\text{-NiFeOOH/PO}_4^{3-}$ surface was significantly increased (Fig. S10, ESI†), which is a major factor leading to the amorphous structure on the $\text{Ru}_{0.1}\text{-NiFeOOH/PO}_4^{3-}$ surface.²⁵ The presence of oxygen vacancies reduces the charge transfer resistance and enhances the charge

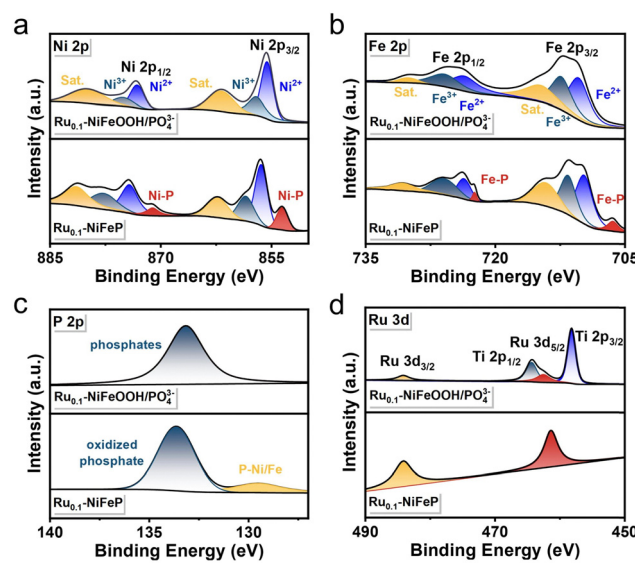


Fig. 2 XPS spectra of (a) Ni 2p, (b) Fe 2p, (c) P 2p and (d) Ru 3d of $\text{Ru}_{0.1}\text{-NiFeOOH/PO}_4^{3-}$ and $\text{Ru}_{0.1}\text{-NiFeP}$.



transfer capability of the catalyst.²⁶ All of the results demonstrate the synthesis of surface amorphization and phosphate functionalization of the Ru_{0.1}-NiFeOOH/PO₄³⁻ electrocatalyst.

The OER performance of the optimized Ru content in Ru_{0.1}-NiFeOOH/PO₄³⁻ (normalized by the catalyst surface area) was first evaluated in a three-electrode cell system (Fig. S11, ESI[†]). Fig. 3a shows the linear sweep voltammetry (LSV) curves of Ru_{0.1}-NiFeOOH/PO₄³⁻, NiFeOOH/PO₄³⁻, Ru_{0.1}-NiFeOOH, and commercial RuO₂ in 1 M KOH + seawater electrolyte. The results show that Ru_{0.1}-NiFeOOH/PO₄³⁻ requires only a low overpotential of 255 mV to achieve 10 mA cm⁻², which is lower than that of NiFeOOH/PO₄³⁻ (315 mV), Ru_{0.1}-NiFeOOH (339 mV), and commercial RuO₂ (343 mV). Fig. S12 (ESI[†]) shows that Ru doping shifts the oxidation-reduction peaks of Ru_{0.1}-NiFeOOH/PO₄³⁻ negatively and enlarges the peak area, indicating enhanced reaction kinetics and more active sites. Meanwhile, the LSV curves normalized by the electrochemical surface area (Fig. S13, ESI[†]) show that Ru_{0.1}-NiFeOOH/PO₄³⁻ has better intrinsic catalytic activity than the other three samples. Fig. 3b shows the catalytic performance of Ru_{0.1}-NiFeOOH/PO₄³⁻ in different electrolytes (1 M KOH, 1 M KOH + 0.5 M NaCl, and 1 M KOH + seawater) (Table S2, ESI[†]). The

results indicate that Ru_{0.1}-NiFeOOH/PO₄³⁻ exhibits similar performance in both 1 M KOH and 1 M KOH + 0.5 M NaCl, and this suggests that the PO₄³⁻ is effective in repelling Cl⁻. Furthermore, the faradaic efficiency of oxygen production for Ru_{0.1}-NiFeOOH/PO₄³⁻ is close to 100% in 1 M KOH + seawater electrolyte (Fig. S14, ESI[†]), implying that the electrical energy applied is predominantly dedicated to facilitating the OER. The Tafel slope of Ru_{0.1}-NiFeOOH/PO₄³⁻ is 47.5 mV dec⁻¹ (Fig. 3c), which is lower than that of NiFeOOH/PO₄³⁻ (77.9 mV dec⁻¹), Ru_{0.1}-NiFeOOH (105.4 mV dec⁻¹), and RuO₂ (111.9 mV dec⁻¹), indicating the fast OER kinetics of the Ru_{0.1}-NiFeOOH/PO₄³⁻ catalyst. Additionally, electrochemical impedance spectroscopy (EIS) shows that Ru_{0.1}-NiFeOOH/PO₄³⁻ exhibits the smallest charge transfer resistance during the OER process (Fig. 3d, inset shows the equivalent circuit diagram and fitted data in Table S3, ESI[†]), proving its higher conductivity and faster charge transfer rate than contrasting samples.

Fig. 3e exhibits the superior stability of Ru_{0.1}-NiFeOOH/PO₄³⁻ in three different electrolytes, particularly under the harsh condition of 6 M KOH + seawater. In contrast, the Ru_{0.1}-NiFeOOH electrode was broken and deactivated within no more than 2 h in the 6 M KOH + seawater electrolyte at 0.5 A cm⁻² (Fig. S15, ESI[†]).

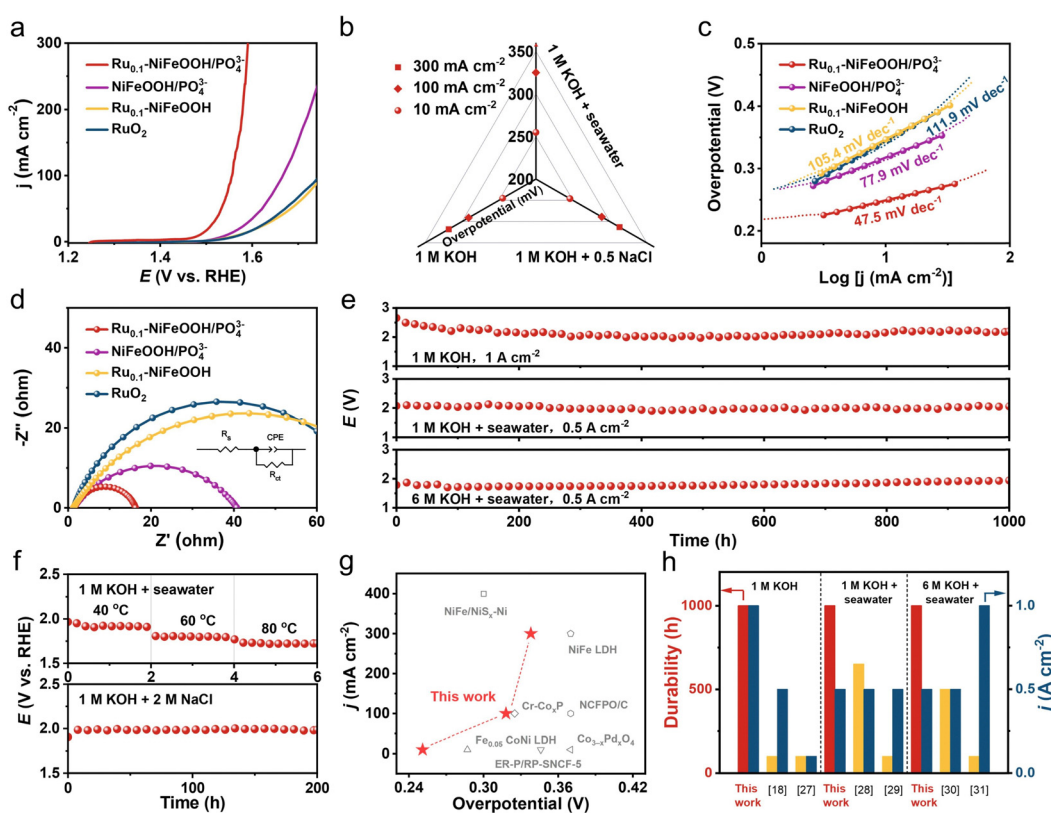


Fig. 3 (a) LSV curves of Ru_{0.1}-NiFeOOH/PO₄³⁻, NiFeOOH/PO₄³⁻, Ru_{0.1}-NiFeOOH and RuO₂ in 1 M KOH + seawater electrolyte. (b) Overpotentials of Ru_{0.1}-NiFeOOH/PO₄³⁻ in three different electrolytes (1 M KOH, 1 M KOH + 0.5 M NaCl, and 1 M KOH + seawater) measured at 10, 100, and 300 mA cm⁻². (c) Tafel plots and (d) EIS spectrum of three different samples tested in 1 M KOH + seawater electrolyte (d inset: fitted equivalent circuit). (e) E-T curves of Ru_{0.1}-NiFeOOH/PO₄³⁻ in 1 M KOH, 1 M KOH + seawater, and 6 M KOH + seawater electrolytes at 1, 0.5, and 0.5 A cm⁻², respectively (conducted at room temperature). (f) E-T curves of Ru_{0.1}-NiFeOOH/PO₄³⁻ in 1 M KOH + seawater electrolyte at various operating temperatures, and in 1 M KOH + 2 M NaCl electrolyte at 0.5 A cm⁻². (g) Overpotential comparison of Ru_{0.1}-NiFeOOH/PO₄³⁻ with reported literature at different current densities with similar seawater conditions. (h) Comparison of Ru_{0.1}-NiFeOOH/PO₄³⁻ with reported literature regarding the duration and working current density.

Fig. 3f and Fig. S16 (ESI[†]) demonstrate that the Ru_{0.1}-NiFeOOH/PO₄³⁻ exhibits superior stability compared to Ru_{0.1}-NiFeOOH at different operating temperatures and in a high chloride concentration electrolyte at 0.5 A cm⁻². We have also investigated the Cl⁻ oxidation of Ru_{0.1}-NiFeOOH and Ru_{0.1}-NiFeOOH/PO₄³⁻ by the iodide titration method. Compared to the electrolyte of Ru_{0.1}-NiFeOOH, which turned yellow after the stability test, the test electrolyte of Ru_{0.1}-NiFeOOH/PO₄³⁻ remained colorless, demonstrating that no oxidative chloride was generated during the stability test (Fig. S17 and S18, ESI[†]).²⁷ These results reveal the effectiveness of the surface functionalization strategy of PO₄³⁻ groups on the catalyst surface. Compared to most of the literature (Fig. 3g, h and Table S4, ESI[†]), the Ru_{0.1}-NiFeOOH/PO₄³⁻ has advantages in terms of overpotential, current density, and stability test time,^{18,27-31} which indicates the significant potential of Ru_{0.1}-NiFeOOH/PO₄³⁻ for industrial applications.

Density functional theory (DFT) calculations were conducted to obtain the free energy according to the typical adsorbate evolution mechanism proposed by Nørskov *et al.* (eqn (S1)–(S4) in the ESI[†]). As shown in Fig. 4a and Fig. S19 (ESI[†]), the Ru_{0.1}-NiFeOOH/PO₄³⁻ model was based on the hypothesis that an amorphous layer forms on the surface of Ru_{0.1}-NiFeOOH after electrochemical activation, where the Ru_{0.1}-NiFeOOH model was built on NiFeOOH, with Ru randomly substituting Ni and Fe atoms. The model of NiFeOOH/PO₄³⁻ features PO₄³⁻

adsorbed on the surface of the NiFeOOH (Fig. S20, ESI[†]). Density of states (DOS) plots (Fig. 4b) show that influenced by the hybridization effect, the formation of the amorphous layer on surface Ru_{0.1}-NiFeOOH/PO₄³⁻ leads to the PDOS transformation of the Ru 3d orbital from discrete peaks to continuous bands. This could potentially provide more adsorption sites and dissociation pathways, facilitating the adsorption and dissociation of intermediates. Consequently, it could enhance the reaction rate. According to the Sabatier principle, an ideal catalyst should exhibit moderate adsorption strength for intermediates. As depicted in Fig. 4c and Fig. S21 (ESI[†]), in the four-step proton-electron paired oxygen evolution reaction, the ideal barrier is 1.23 V. The amorphous Ru_{0.1}-NiFeOOH/PO₄³⁻ exhibits a lower Gibbs free energy compared to the Ru_{0.1}-NiFeOOH and NiFeOOH/PO₄³⁻. Compared to the fourth rate-determining step (OOH* → O₂) of Ru_{0.1}-NiFeOOH, the amorphous Ru_{0.1}-NiFeOOH/PO₄³⁻ shifted the rate-determining step to the third step (O* → OOH*), accompanied by a significant barrier reduction (from 1.92 eV to 1.70 eV). Additionally, compared to NiFeOOH/PO₄³⁻, the rate-determining step for the Ru_{0.1}-NiFeOOH/PO₄³⁻ catalyst changes from OH⁻ → OH* to O* → OOH*. This change may be due to the doping of Ru atoms, further resulting in lattice distortion. The distortion of the catalyst can alter the surface structure and provide more favorable adsorption sites for the reactants. This shift facilitated the effective progression of the OER. As shown in Fig. 4d, the amorphous

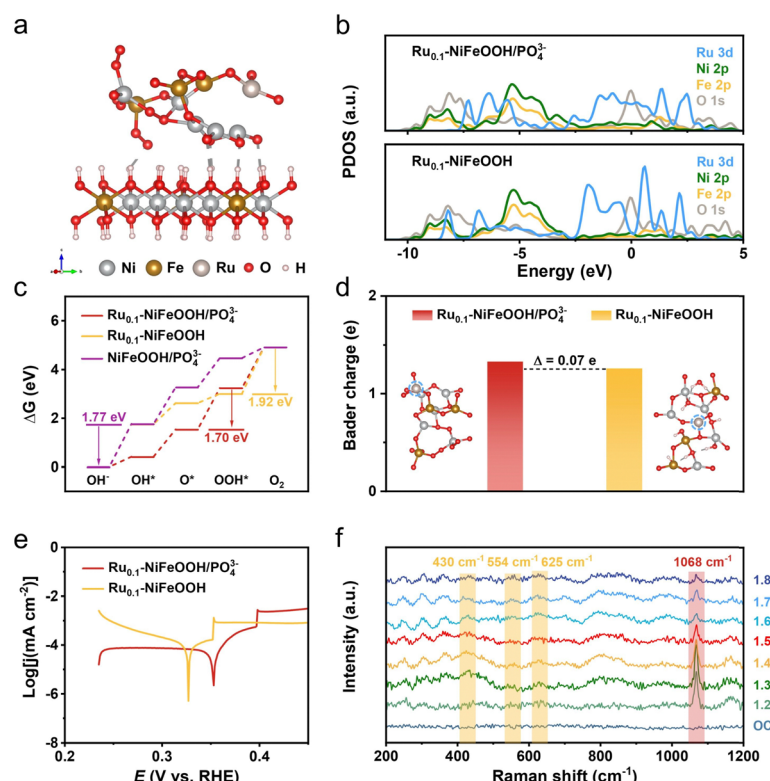


Fig. 4 (a) Model of Ru_{0.1}-NiFeOOH/PO₄³⁻ with surface amorphization treatment. (b) Density of states comparison chart for Ru_{0.1}-NiFeOOH/PO₄³⁻ and Ru_{0.1}-NiFeOOH. (c) Calculated free energy diagrams of Ru_{0.1}-NiFeOOH/PO₄³⁻, Ru_{0.1}-NiFeOOH and NiFeOOH/PO₄³⁻ models for the OER. (d) Bader charge of the Ru site in Ru_{0.1}-NiFeOOH/PO₄³⁻ and Ru_{0.1}-NiFeOOH, respectively. (e) Tafel plots of Ru_{0.1}-NiFeOOH/PO₄³⁻ and Ru_{0.1}-NiFeOOH in a 1.0 M KOH + seawater electrolyte. (f) *In situ* Raman spectra of Ru_{0.1}-NiFeOOH/PO₄³⁻ in 1.0 M KOH electrolyte.



$\text{Ru}_{0.1}\text{-NiFeOOH}/\text{PO}_4^{3-}$ has more unsaturated or dangling bonds than $\text{Ru}_{0.1}\text{-NiFeOOH}$, leading to an increase in surface charges. This modification in surface characteristics intensifies the electrostatic interactions between the catalyst's surface and various reaction intermediates such as OH^- , O^* , and OOH^* .³² Fig. 4e shows that the $\text{Ru}_{0.1}\text{-NiFeOOH}/\text{PO}_4^{3-}$ exhibits a more positive corrosion potential than that of the $\text{Ru}_{0.1}\text{-NiFeOOH}$. These findings indicate that the adsorption of PO_4^{3-} on the $\text{Ru}_{0.1}\text{-NiFeOOH}$ surface can effectively repel Cl^- from seawater, thereby enhancing the catalyst stability.

In situ Raman spectra are shown in Fig. 4f, no distinct characteristic peaks were detected at open-circuit voltage due to strong scattering from the electrolyte and weak signals from the sample itself. After applying 1.23 V for 25 minutes, a new peak emerged at 1068 cm^{-1} , indicating the oxidation of P to PO_4^{3-} in the $\text{Ru}_{0.1}\text{-NiFeOOH}/\text{PO}_4^{3-}$ sample.^{33,34} Concurrently, a weaker peak at $\sim 248\text{ cm}^{-1}$ corresponding to the Ni–O/Fe–O vibration mode in the NiFeOOH appeared, suggesting that the oxidation of P atoms caused some PO_4^{3-} to dissolve in the electrolyte, creating a favorable environment for the bonding of Ni and Fe sites with OH^- .^{35,36} As the voltage increased further (from 1.30 to 1.80 V vs. RHE), more emerging characteristic peaks located at 306, 365, 430, 554, 625, 699, 800, and 988 cm^{-1}

were detected in the Raman spectra. The peaks at 430, 554, and 625 cm^{-1} correspond to lattice vibrations of NiFeOOH,^{37,38} and the peaks at 306 and 699 cm^{-1} correspond to various Ni–O/Fe–O bond vibrations of $\text{Ni}(\text{Fe})(\text{OH})_2$.^{39,40} Meanwhile, the intensity of the peak at 1068 cm^{-1} continuously decreased with rising voltage, indicating the gradual dissolution of PO_4^{3-} into the electrolyte, further suggesting the transformation of PO_4^{3-} sites into hydroxide/hydroxide oxide structures occupied by OH^- or OOH^- .²⁰ The literature indicates that vibrational signals at 365 and 699 cm^{-1} can be attributed to the NiFe_2O_4 spinel structure, present in the evolution cycle of $\text{Ni}^{2+}/\text{Ni}^{3+}$ and $\text{Fe}^{2+}/\text{Fe}^{3+}$ active sites.²¹ Additionally, the characteristic peaks at 800 and 990 cm^{-1} , similar to many *in situ* spectra reported in the literature,^{41,42} are attributed to the fluorescence background of the alkaline solution and the P–O bond stretching vibrations of dissolved phosphate.^{43,44} Compared to $\text{NiFeOOH}/\text{PO}_4^{3-}$ (Fig. S22, ESI†), the $\text{Ru}_{0.1}\text{-NiFeOOH}/\text{PO}_4^{3-}$ catalyst exhibits a lower onset potential and a larger peak area for the NiFeOOH phase. This may be attributed to the Ru doping, which could induce lattice distortion and promote the structural evolution towards NiFeOOH, thereby accelerating the OER process. In summary, the *in situ* Raman spectra confirm the evolution of $\text{Ru}_{0.1}\text{-NiFeOOH}/\text{PO}_4^{3-}$ into corresponding hydroxide and hydroxide oxide active species during the OER process.

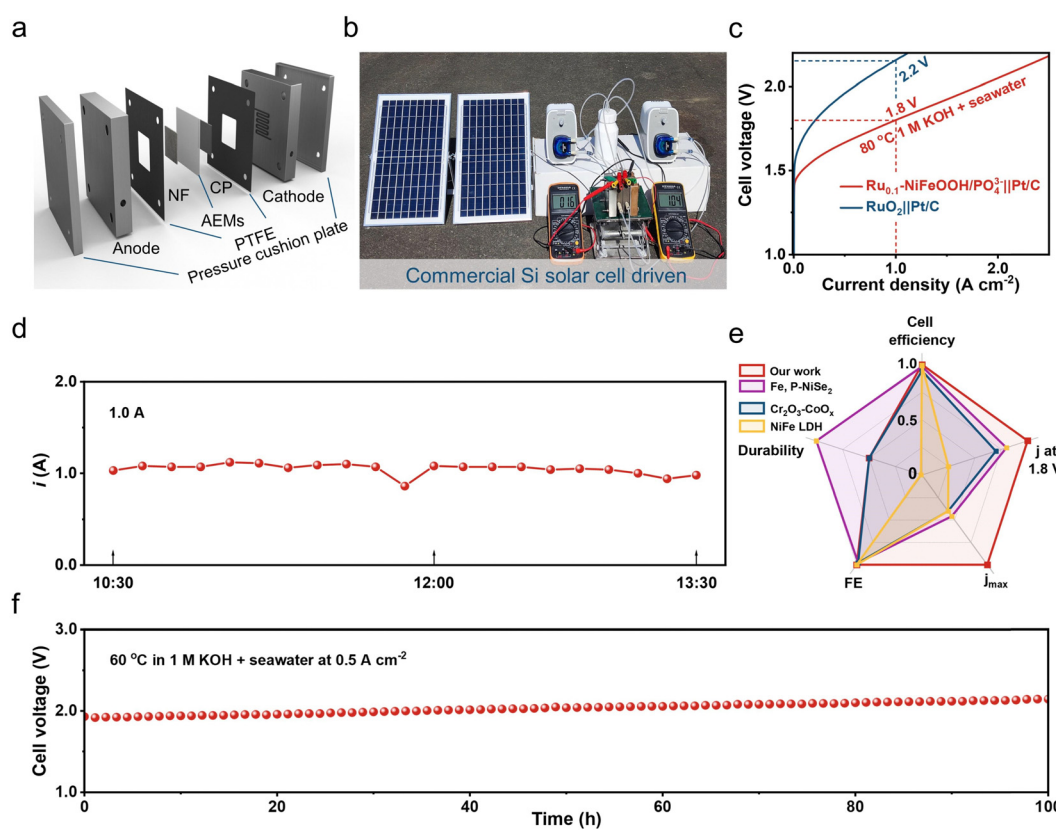


Fig. 5 (a) Schematic of an AEM electrolyzer. (b) Photograph of a commercial silicon-based solar panel powering a $\text{Ru}_{0.1}\text{-NiFeOOH}/\text{PO}_4^{3-}\text{||Pt/C}$ AEM electrolyzer. (c) Polarization curves of $\text{Ru}_{0.1}\text{-NiFeOOH}/\text{PO}_4^{3-}\text{||Pt/C}$ normalized to electrode area in $1\text{ M KOH} + \text{seawater}$ at $80\text{ }^\circ\text{C}$, compared with commercial $\text{RuO}_2\text{||Pt/C}$. (d) $I\text{-}T$ curve of the AEM electrolyzer powered by a commercial silicon-based solar panel at 1.0 A (conducted at room temperature). (e) Radar chart comparisons of the normalized comprehensive performance of the $\text{Ru}_{0.1}\text{-NiFeOOH}/\text{PO}_4^{3-}\text{||Pt/C}$ electrolyzer with reported literature. (f) $E\text{-}T$ curve of the $\text{Ru}_{0.1}\text{-NiFeOOH}/\text{PO}_4^{3-}\text{||Pt/C}$ electrolyzer at $60\text{ }^\circ\text{C}$ in $1\text{ M KOH} + \text{seawater}$ electrolyte at 0.5 A cm^{-2} .



To evaluate the practical use of the $\text{Ru}_{0.1}\text{-NiFeOOH}/\text{PO}_4^{3-}$ catalyst, we assembled it in an AEM electrolyzer and powered the electrolyzer by solar energy. The results show that the electrolyzer required only 1.6 V to achieve 0.5 A cm^{-2} in 6 M KOH + seawater electrolyte (Fig. 5a and b), demonstrating the best performance among most of the literature (Table S5 and Fig. S23, ESI†). The electrolyzer only needs 1.8 V to achieve 1.0 A cm^{-2} , superior to that of the commercial RuO_2 -based AEM electrolyzer (2.2 V). During the stability test of the $\text{Ru}_{0.1}\text{-NiFeOOH}/\text{PO}_4^{3-}$ catalyst assembled electrolyzer (Fig. 5c), the working current is maintained at 1.0 A using a regulator, and the electrolyzer could operate stably at 1.0 A for a long time (Fig. 5d). Compared with the reported literature (Fig. 5e, f and Table S6, ESI†),^{15,45,46} The $\text{Ru}_{0.1}\text{-NiFeOOH}/\text{PO}_4^{3-}$ exhibits the advantages of low-applied voltage and superior stability at high current density, despite a certain increase in potential due to temperature loss. These results show the promise of $\text{Ru}_{0.1}\text{-NiFeOOH}/\text{PO}_4^{3-}$ as an efficient and stable catalyst for industrial seawater electrolysis.

Conclusion

We have developed a dual-optimized function $\text{Ru}_{0.1}\text{-NiFeOOH}/\text{PO}_4^{3-}$ catalyst for robust seawater electrolysis. First, we employed a trace Ru doping strategy to accelerate the amorphization of the NiFeOOH surface, potentially enhancing the active site availability and thereby improving the catalytic performance of $\text{Ru}_{0.1}\text{-NiFeOOH}/\text{PO}_4^{3-}$. Second, we introduced PO_4^{3-} to resist Cl^- corrosion on the $\text{Ru}_{0.1}\text{-NiFeOOH}$ surface, acting as an anion protective layer and achieving long-lasting seawater oxidation at high current density. Notably, the $\text{Ru}_{0.1}\text{-NiFeOOH}/\text{PO}_4^{3-}$ electrode remains stable up to 1000 h at 1.0, 0.5, and 0.5 A cm^{-2} in 1 M KOH, 1 M KOH + seawater, and 6 M KOH + seawater electrolytes, respectively. We assembled the $\text{Ru}_{0.1}\text{-NiFeOOH}/\text{PO}_4^{3-}$ in an AEM electrolyzer, which requires only 1.8 V to achieve 1.0 A cm^{-2} under industrial conditions. When the AEM electrolyzer is powered by solar energy, this system only needs 1.6 V to achieve 0.5 A cm^{-2} , promising for the production of green H_2 from renewable energy. Taken together, we believe that the surface synthetic strategy developed in this work will have a significant impact on seawater electrolysis technology and make a substantial contribution to global H_2 energy development and sustainable energy utilization.

Author contributions

H. W.: data curation, formal analysis, investigation, methodology, visualization, writing – original draft; N. N. J. and B. H.: writing – review & editing, methodology; Q. M. Y. and L. H. G.: resources, supervision, writing – review & editing. All authors read and commented on the manuscript.

Data availability

The data that support the findings of this study are available from the corresponding author, upon reasonable request.

Conflicts of interest

There are no conflicts to declare.

Acknowledgements

We acknowledge financial support from the National Natural Science Foundation of China (no. 22171266 and 52303375) and the Shenzhen Basic Research Project (no. WDZC202208121 41108001).

References

- 1 D. Shindell and C. J. Smith, *Nature*, 2019, **573**, 408.
- 2 Y. J. Wang, R. Wang, K. Tanaka, P. Ciais, J. Penuelas, Y. Balkanski, J. Sardans, D. Hauglustaine, W. Liu, X. Xing, J. Li, S. Xu, Y. Xiong, R. Yang, J. Cao, J. Chen, L. Wang, X. Tang and R. Zhang, *Nature*, 2023, **619**, 761.
- 3 J. A. Turner, *Science*, 2004, **305**, 972.
- 4 S. van Renssen, *Nat. Clim. Change*, 2020, **10**, 799.
- 5 A. J. Shih, M. C. O. Monteiro, F. Dattila, D. Pavesi, M. Philips, A. H. M. da Silva, R. E. Vos, K. Ojha, S. Park, O. van der Heijden, G. Marcandalli, A. Goyal, M. Villalba, X. Chen, G. T. K. K. Gunasooriya, I. McCrum, R. Mom, N. López and M. T. M. Koper, *Nat. Rev. Methods Primers*, 2022, **2**, 84.
- 6 H. Liu, X. Kang, T. Zhao, Z. Zhang, S. Ge, S. Hu, Y. Luo, F. Yang, S. H. Li, C. Sun, Q. Yu, H. M. Cheng and B. Liu, *Sci. China Mater.*, 2022, **65**, 3243.
- 7 M. A. Khan, T. Al-Attas, S. Roy, M. M. Rahman, N. Ghaffour, V. Thangadurai, S. Larter, J. Hu, P. M. Ajayan and M. G. Kibria, *Energy Environ. Sci.*, 2021, **14**, 4831.
- 8 Y. Kuang, M. J. Kenney, Y. Meng, W.-H. Hung, Y. Liu, J. E. Huang, R. Prasanna, P. Li, Y. Li, L. Wang, M.-C. Lin, M. D. McGehee, X. Sun and H. Dai, *Proc. Natl. Acad. Sci. U. S. A.*, 2019, **116**, 6624.
- 9 M. Al-Abri, B. Al-Ghafri, T. Bora, S. Dobretsov, J. Dutta, S. Castelletto, L. Rosa and A. Boretti, *npj Clean Water*, 2019, **2**, 2.
- 10 S. Ge, R. Xie, B. Huang, Z. Zhang, H. Liu, X. Kang, S. Hu, S. Li, Y. Luo, Q. Yu, J. Wang, G. Chai, L. Guan, H. M. Cheng and B. Liu, *Energy Environ. Sci.*, 2023, **16**, 3734.
- 11 S. Hu, S. Ge, H. Liu, X. Kang, Q. Yu and B. Liu, *Adv. Funct. Mater.*, 2022, **32**, 2201726.
- 12 H. Xie, Z. Zhao, T. Liu, Y. Wu, C. Lan, W. Jiang, L. Zhu, Y. Wang, D. Yang and Z. Shao, *Nature*, 2022, **612**, 673.
- 13 X. Kang, F. Yang, Z. Zhang, H. Liu, S. Ge, S. Hu, S. Li, Y. Luo, Q. Yu, Z. Liu, Q. Wang, W. Ren, C. Sun, H.-M. Cheng and B. Liu, *Nat. Commun.*, 2023, **14**, 3607.
- 14 H. Liu, W. Shen, H. Jin, J. Xu, P. Xi, J. Dong, Y. Zheng and S. Z. Qiao, *Angew. Chem., Int. Ed.*, 2023, **62**, e202311674.



15 S. Dresp, T. Ngo Thanh, M. Klingenhof, S. Brückner, P. Hauke and P. Strasser, *Energy Environ. Sci.*, 2020, **13**, 1725.

16 L. Tan, J. Yu, C. Wang, H. Wang, X. Liu, H. Gao, L. Xin, D. Liu, W. Hou and T. Zhan, *Adv. Funct. Mater.*, 2022, **32**, 2200951.

17 Y. Yang, W. H. Lie, R. R. Unocic, J. A. Yuwono, M. Klingenhof, T. Merzdorf, P. W. Buchheister, M. Kroschel, A. Walker, L. C. Gallington, L. Thomsen, P. V. Kumar, P. Strasser, J. A. Scott and N. M. Bedford, *Adv. Mater.*, 2023, **35**, 2305573.

18 L. Yu, J. Y. Xiao, C. Q. Huang, J. Q. Zhou, M. Qiu, Y. Yu, Z. F. Ren, C. W. Chu and J. C. Yu, *Proc. Natl. Acad. Sci. U. S. A.*, 2022, **119**, e2202382119.

19 L. Shao, X. Han, L. Shi, T. Wang, Y. Zhang, Z. Jiang, Z. Yin, X. Zheng, J. Li, X. Han and Y. Deng, *Adv. Energy Mater.*, 2023, **14**, 2303261.

20 P. Yan, Q. Liu, H. Zhang, L. Qiu, H. B. Wu and X.-Y. Yu, *J. Mater. Chem. A*, 2021, **9**, 15586.

21 Y. Li, Y. Wu, H. Hao, M. Yuan, Z. Lv, L. Xu and B. Wei, *Appl. Catal., B*, 2022, **305**, 121033.

22 F. Hu, S. L. Zhu, S. M. Chen, Y. Li, L. Ma, T. P. Wu, Y. Zhang, C. M. Wang, C. C. Liu, X. J. Yang, L. Song, X. W. Yang and Y. J. Xiong, *Adv. Mater.*, 2017, **29**, 1606570.

23 A. P. Grosvenor, S. D. Wik, R. G. Cavell and A. Mar, *Inorg. Chem.*, 2005, **44**, 8988.

24 Z. Y. He, J. Zhang, Z. H. Gong, H. Lei, D. Zhou, N. Zhang, W. J. Mai, S. J. Zhao and Y. Chen, *Nat. Commun.*, 2022, **13**, 2191.

25 J. S. Qu, W. Liu, R. Z. Liu, J. D. He, D. D. Liu, Z. C. Feng, Z. D. Feng, R. G. Li and C. Li, *Chem Catal.*, 2023, **3**, 100759.

26 H. Y. Zhang, L. L. Wu, R. H. Feng, S. H. Wang, C.-S. Hsu, Y. M. Ni, A. Ahmad, C. R. Zhang, H. F. Wu, H.-M. Chen, W. Zhang, Y. Li, P. Liu and F. Song, *ACS Catal.*, 2023, **13**, 6000–6012.

27 H. You, D. Wu, D. Si, M. Cao, F. Sun, H. Zhang, H. Wang, T. F. Liu and R. Cao, *J. Am. Chem. Soc.*, 2022, **144**, 9254.

28 L. Wu, F. Zhang, S. Song, M. Ning, Q. Zhu, J. Zhou, G. Gao, Z. Chen, Q. Zhou, X. Xing, T. Tong, Y. Yao, J. Bao, L. Yu, S. Chen and Z. Ren, *Adv. Mater.*, 2022, **34**, 2201774.

29 L. Yu, L. Wu, B. McElhenny, S. Song, D. Luo, F. Zhang, Y. Yu, S. Chen and Z. Ren, *Energy Environ. Sci.*, 2020, **13**, 3439.

30 L. Wu, L. Yu, Q. Zhu, B. McElhenny, F. Zhang, C. Wu, X. Xing, J. Bao, S. Chen and Z. Ren, *Nano Energy*, 2021, **83**, 105838.

31 X. Wang, X. Liu, S. Wu, K. Liu, X. Meng, B. Li, J. Lai, L. Wang and S. Feng, *Nano Energy*, 2023, **109**, 108292.

32 S. Li, R. Ma, J. Hu, Z. Li, L. Liu, X. Wang, Y. Lu, G. E. Sterbinsky, S. Liu, L. Zheng, J. Liu, D. Liu and J. Wang, *Nat. Commun.*, 2022, **13**, 2916.

33 X. Chen, K. Xu, J. Li, X. Wang, T. Zhao, F. Liu, M. Yu and F. Cheng, *Chin. Chem. Lett.*, 2023, **34**, 108713.

34 X. Liu, J. Huang, T. Li, W. Chen, G. Chen, L. Han and K. Ostrikov, *J. Mater. Chem. A*, 2022, **10**, 13448.

35 L. Wei, M. Du, R. Zhao, F. Lv, L. Li, L. Zhang, D. Zhou and J. Su, *J. Mater. Chem. A*, 2022, **10**, 23790.

36 P. Zhou, S. Chen, H. Bai, C. Liu, J. Feng, D. Liu, L. Qiao, S. Wang and H. Pan, *J. Colloid Interface Sci.*, 2023, **647**, 65.

37 Q. Li, Q. Chen, S. Lei, M. Zhai, G. Lv, M. Cheng, L. Xu, H. Xu, Y. Deng and J. Bao, *J. Colloid Interface Sci.*, 2023, **631**, 56.

38 Y. Wu, Z. Xie, Y. Li, Z. Lv, L. Xu and B. Wei, *Int. J. Hydrogen Energy*, 2021, **46**, 25070.

39 J. Xu, B.-X. Wang, D. Lyu, T. Wang and Z. Wang, *Int. J. Hydrogen Energy*, 2023, **48**, 10724.

40 F. Tang, T. Liu, W. Jiang and L. Gan, *J. Electroanal. Chem.*, 2020, **871**, 114282.

41 O. Diaz-Morales, D. Ferrus-Suspedra and M. T. M. Koper, *Chem. Sci.*, 2016, **7**, 2639.

42 Z. Qiu, Y. Ma and T. Edvinsson, *Nano Energy*, 2019, **66**, 104118.

43 R. I. Bickley, H. G. M. Edwards, R. E. Gustarb and J. K. F. Tait, *Mol. Struct.*, 1992, **273**, 61.

44 C. A. Melendres, N. Camillone III and T. Tipton, *Electrochim. Acta*, 1989, **34**, 281.

45 J.-F. Chang, G.-Z. Wang, Z.-Z. Yang, B.-Y. Li, Q. Wang, R. Kuliev, N. Orlovskaya, M. Gu, Y.-G. Du, G.-F. Wang and Y. Yang, *Adv. Mater.*, 2021, **33**, 2101425.

46 J. Guo, Y. Zheng, Z. Hu, C. Zheng, J. Mao, K. Du, M. Jaroniec, S.-Z. Qiao and T. Ling, *Nat. Energy*, 2023, **8**, 264.

